Inorganic Chemistry

Article

pubs.acs.org/IC

Substituent Effects on Core Structures and Heterogeneous Catalytic Activities of $Mn^{III}(\mu\text{-}O)_2Mn^{IV}$ Dimers with 2,2′:6′,2″-Terpyridine Derivative Ligands for Water Oxidation

Hirosato Yamazaki,[†] Satoshi Igarashi,[‡] Toshi Nagata,[§] and Masayuki Yagi*[,†,∥]

[†]Department of Materials Science and Technology, Faculty of Engineering and Center for Transdisciplinary Research, Niigata University, 8050 Ikarashi-2, Niigata 950-2181, Japan

[‡]Faculty of Education, Niigata University, 8050 Ikarashi-2, Niigata 950-2181, Japan

[§]Institute for Molecular Science, Myodaiji, Okazaki 444-8787, Japan

[∥]PRESTO (Precursory Research for Embryonic Science and Technology), Japan Science and Technology Agency (JST), 4-1-8 Honcho, Kawaguchi, Saitama 332-0012, Japan

Supporting Information

ABSTRACT: $[(OH_2)(R\text{-terpy})Mn(\mu\text{-}O)_2Mn(R\text{-terpy})(OH_2)]^{3+}$ (R-terpy = 4′-substituted 2,2′:6′,2″-terpyridine, R = butoxy (BuO), propoxy (PrO), ethoxy (EtO), methoxy (MeO), methyl (Me), methylthio (MeS), chloro (Cl)) have been synthesized as a functional oxygen-evolving complex (OEC) model and characterized by UV−vis and IR spectroscopic, X-ray crystallographic, magnetometric, and electrochemical techniques. The UV−vis spectra of derivatives in water were hardly influenced by the 4′-substituent variation. X-ray crystallographic data showed that Mn centers in the $Mn^{III}(\mu\text{-}O)_2Mn^{IV}$ cores for derivatives with R = H, MeS, Me, EtO, and BuO are crystallographically indistinguishable, whereas the derivatives with R = MeO and PrO gave the significantly distinguishable Mn centers in the cores. The indistinguishable Mn centers could be caused by rapid electron exchange between the Mn centers to result in the delocalized $Mn(\mu\text{-}O)_2Mn$ core. The exchange integral values (J = −196 to −178 cm^{-1}) for delocalized cores were lower than that (J = −163 to −161 cm^{-1}) for localized cores, though the Mn···Mn distances are nearly the same (2.707−2.750 Å). The half wave potential ($E_{1/2}$) of a Mn^{III}−Mn^{IV}/Mn^{IV}−Mn^{IV} pair of the derivatives decreased with an increase of the electron-donating ability of the substituted groups for the delocalized core, but it deviated from the correlation for the localized cores. The catalytic activities of the derivatives on mica for heterogeneous water oxidation were remarkably changed by the substituted groups. The second order rate constant (k_2/mol^{-1} s^{-1}) for O_2 evolution was indicated to be correlated to $E_{1/2}$ of a Mn^{III}−Mn^{IV}/Mn^{IV}−Mn^{IV} pair; k_2 increased by a factor of 29 as $E_{1/2}$ increased by 28 mV.

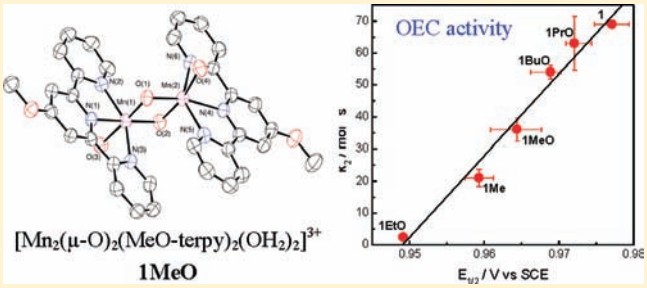

INTRODUCTION

The oxidation of water to form O_2 in green plants and cyanobacteria is catalyzed by the OEC of photosystem II (PS II).[1,2] Recent X-ray diffraction and extended X-ray absorption fine structure (EXAFS) studies have considerably revealed the detailed structure of the OEC.[3−9] Very recently, the crystal structure of PS II at a resolution of 1.9 Å was reported, in which all of the metal atoms of the Mn_4CaO_5 cluster are located together with all of their ligands in the OEC center. Five oxygen atoms in the cluster were found to serve as oxo bridges linking the five metal atoms.[9] X-ray crystallography, EXAFS, electron paramagnetic resonance, and magnetic susceptibility studies on synthetic manganese complexes have provided important insights about the OEC in PS II.[10−16] However, only a few complexes act as a functional model that is capable of catalyzing water oxidation.[17−28]

Water oxidation chemistry by synthetic manganese complexes has undoubtedly brightened up since O_2 evolution by $[(H_2O)(terpy)Mn(\mu\text{-}O)_2Mn(terpy)(H_2O)]^{3+}$ (terpy = 2,2′:6′,2″-terpyridine) (**1**) in a homogeneous aqueous solution was reported nearly a decade ago.[21,22] Our previous work demonstrated that **1** catalyzes water oxidation to evolve O_2 when **1** is adsorbed on layer compounds.[19,20,29] It illustrated a successful design of a functional OEC model by adsorbing **1** onto layer compounds. Recently, visible-light-derived O_2 production was yielded by conjugating water oxidation catalysis by **1** and photosensitization of $[Ru(bpy)_3]^{2+}$ (bpy = 2,2′-bipyridine) at an interlayer of mica.[30] The kinetic analysis of O_2 evolution suggested that 2 equiv of **1** adsorbed on layer compounds is required in the cooperative catalysis for water oxidation.[19,20] It is revealed that the catalytic activity of **1** depends on the concentration of **1** adsorbed on layer compounds as well as its adsorption conditions such as a layer structure and cation

Received: August 22, 2011
Published: January 26, 2012

 © 2012 American Chemical Society dx.doi.org/10.1021/ic201797h | *Inorg. Chem.* 2012, 51, 1530−1539

exchange capacity (CEC). However, the effect on the catalytic activity for heterogeneous water oxidation on a change in the substituent present in derivatives of **1** has not yet been studied. In our preliminary work, $[(OH_2)(Cl\text{-terpy})Mn(\mu\text{-}O)_2Mn(Cl\text{-terpy})(OH_2)]^{3+}$ (Cl-terpy = 4′-chloro-2,2′:6′,2″-terpyridine) cannot act as a catalyst for water oxidation on mica.[31] This result allows us to predict that the catalytic activities of derivatives of **1** on mica for water oxidation are influenced by 4′-substituent variation on terpy ligands. To test the prediction, the detailed studies are requested using a series of derivatives of **1**. It could provide important insights into the structure and the mechanism of water oxidation at OEC. It could also be available as indirect evidence that **1** derivatives act as a molecular catalyst and not through its decomposition to metal oxides on layer compounds, as recently discussed for the Mn_4O_4 catalyst immobilized in a Nafion membrane.[32]

The pioneering work on synthesis of **1** derivatives was previously reported by Chen et al.[33]

However, influence of the substituted terpy ligands on geometrical and electronic structures of the $Mn(\mu\text{-}O)_2Mn$ core has not been investigated yet due to difficulty in isolation and crystallization of the **1** derivatives, although a single derivative of $[(OH_2)(MS\text{-terpy})Mn(\mu\text{-}O)_2Mn(MS\text{-terpy})(OH_2)](NO_3)_3$ (**1MS**$(NO_3)_3$) (MS-terpy = 4′-mesityl-2,2′:6′,2″-terpyridine) was characterized by X-ray diffraction crystallography. In the present study, a series of $[(OH_2)(R\text{-terpy})Mn(\mu\text{-}O)_2Mn(R\text{-terpy})(OH_2)](NO_3)_3$ derivatives with various 4′-substituted terpy (R-terpy) ligands (Chart 1) have been isolated and characterized by a X-ray crystallographic, magnetic susceptibility, and electrochemical measurement. The catalytic activities of the derivatives on mica for the heterogeneous water oxidation are demonstrated to be remarkably changed by substituent variation on terpy ligands. The substituent effect on the catalytic activity as well as geometrical and electric structures of the $Mn(\mu\text{-}O)_2Mn$ core will be comprehensively discussed.

Chart 1. Structures of $[(OH_2)(R\text{-terpy})Mn(\mu\text{-}O)_2Mn(R\text{-terpy})(OH_2)]^{3+}$ Derivatives

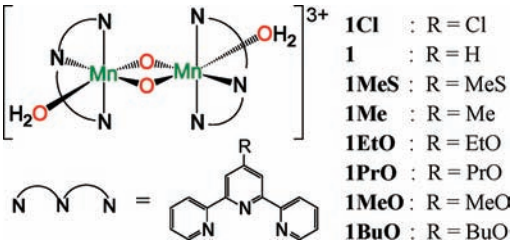

EXPERIMENTAL SECTION

Materials. BuO-terpy,[34] PrO-terpy,[34] EtO-terpy,[35] MeO-terpy,[35] Me-terpy,[36] MeS-terpy,[36] and Cl-terpy[37] were synthesized according to the literature. $Mn(NO_3)_2$, $KMnO_4$, and $Ce(NH_4)_2(NO_3)_6$ (Wako Pure Chemical Industries, Ltd.), and terpy (Aldrich), were purchased and used as received. Somasif (ME-100) of mica was given from Co-op Chemical Co., Inc., Japan, and used without further purification.

Preparations. *$[(OH_2)(terpy)Mn(\mu\text{-}O)_2Mn(terpy)(OH_2)](NO_3)_3$ (1-$(NO_3)_3$).* **1**$(NO_3)_3$ was prepared according to the literature.[19,20] Yield: 88.5%. UV−vis spectrum (H_2O): λ_{max} (ε) = 551 (605), 655 (600 M^{-1} cm^{-1}). IR in cm^{-1} (KBr): ν = 3431 (m), 3068 (m), 1598 (m), 1573 (m), 1477 (m), 1451 (m), 1384 (s), 1363 (s), 1287 (s), 1024 (s), 831 (w), 807 (w), 780 (s), 711 (w), 698 (m), 640 (m), 603 (m).

$[(OH_2)(MeS\text{-terpy})Mn(\mu\text{-}O)_2Mn(MeS\text{-terpy})(OH_2)](NO_3)_3$ (1MeS$(NO_3)_3$). **1MeS**$(NO_3)_3$ was synthesized with reference to the preparation method of **1**$(NO_3)_3$. $Mn(NO_3)_2$ (49.4 mg, 0.172 mmol) and MeS-terpy (48.1 mg, 0.172 mmol) were mixed in 4 mL of water (pH = 2.0). A 516 μL portion of a 0.1 M $KMnO_4$ aqueous solution was delivered by drops into the solution very slowly. It was stirred over 4 h to give a dark green solution including a little brown precipitate. After the precipitate was removed by centrifugation, a cold saturated KNO_3 aqueous solution (0.1 mL) was added to the solution very slowly, and then cooled to 5 °C. The dark green microcrystalline **1MeS**$(NO_3)_3$ was filtered and washed with ice water and diethylether. Recrystallization from water (pH = 4.0) yielded dark-green blocks. Yield: 35.9 mg (45.2%). Anal. $C_{32}H_{30}Mn_2N_9O_{13}S_2$, **1MeS**$(NO_3)_3$, Calcd: C 41.66%, H 3.28%, N 13.66%. Found: C 41.79%, H 3.18%, N 13.78%. UV−vis spectrum (H_2O): λ_{max} (ε) = 552 (616), 655 (604 M^{-1} cm^{-1}). IR in cm^{-1} (KBr): ν = 3419 (m), 3061 (w), 1597 (s), 1567 (m), 1537 (m), 1476 (s), 1385 (s), 1285 (m), 1019 (m), 832 (m), 793 (m), 700 (w), 619 (w).

$[(OH_2)(Me\text{-terpy})Mn(\mu\text{-}O)_2Mn(Me\text{-terpy})(OH_2)](NO_3)_3$ (1Me$(NO_3)_3$). **1Me**$(NO_3)_3$ was prepared similarly to **1MeS**$(NO_3)_3$ using Me-terpy (49.4 mg, 0.172 mmol) instead of MeS-terpy. However, 1.3 mL of the solvent (water) was used due to the higher solubility of **1Me**$(NO_3)_3$. Yield: 32.5 mg (44.0%). Anal. $C_{32}H_{34}Mn_2N_9O_{15}$, **1Me**$(NO_3)_3{\cdot}2H_2O$, Calcd: C 42.97%, H 3.83%, N 14.09%. Found: C 42.74%, H 3.57%, N 14.26%. UV−vis spectrum (H_2O): λ_{max} (ε) = 551 (619), 655 (608 M^{-1} cm^{-1}). IR in cm^{-1} (KBr): ν = 3419 (m), 3060 (m), 1598 (m), 1569 (w), 1477 (m), 1384 (s), 1020 (m), 832 (m), 794 (m), 702 (m), 639 (w), 619 (w). The crystal was obtained as **1Me**·2[Mn(Me-terpy)-$(NO_3)(H_2O)_2](NO_3)$·$6(H_2O)$ from 1.3 mL of an aqueous solution, 0.172 mmol $Mn(NO_3)_2$, 0.172 mmol Me-terpy, and 0.026 mmol $KMnO_4$.

$[(OH_2)(EtO\text{-terpy})Mn(\mu\text{-}O)_2Mn(EtO\text{-terpy})(OH_2)](NO_3)_3$ (1EtO-$(NO_3)_3$). **1EtO**$(NO_3)_3$ was prepared similarly to **1MeS**$(NO_3)_3$ using EtO-terpy (47.7 mg, 0.172 mmol). Yield: 47.2 mg (59.7%). Anal. $C_{34}H_{37}Mn_2N_9O_{16.5}$, **1EtO**$(NO_3)_3{\cdot}1.5H_2O$, Calcd: C 43.19%, H 3.94%, N 13.33%. Found: C 43.02%, H 3.95%, N 13.35%. UV−vis spectrum (H_2O): λ_{max} (ε) = 552 (620), 655 (598 M^{-1} cm^{-1}). IR in cm^{-1} (KBr): ν = 3418 (m), 3066 (w), 1614 (s), 1557 (m), 1481 (m), 1441 (m), 1384 (s), 1227 (s), 1165 (m), 1058 (m), 1036 (m), 796 (m), 705 (m), 638 (m), 619 (m).

$[(OH_2)(PrO\text{-terpy})Mn(\mu\text{-}O)_2Mn(PrO\text{-terpy})(OH_2)](NO_3)_3$ (1PrO-$(NO_3)_3$). **1PrO**$(NO_3)_3$ was prepared similarly to **1MeS**$(NO_3)_3$ using PrO-terpy (50.1 mg, 0.172 mmol). However, 1 mL of hot acetone was used as solvent to dissolve PrO-terpy. Yield: 48.2 mg (59.1%). Anal. $C_{36}H_{38}Mn_2N_9O_{15}$, **1PrO**$(NO_3)_3$, Calcd: C 45.68%, H 4.05%, N 13.32%. Found: C 45.77%, H 4.23%, N 13.36%. UV−vis spectrum (H_2O): λ_{max} (ε) = 552 (610), 655 (603 M^{-1} cm^{-1}). IR in cm^{-1} (KBr): ν = 3420 (m), 3066 (w), 2971 (w), 1613 (s), 1557 (m), 1481 (m), 1440 (m), 1384 (s), 1227 (s), 1164 (m), 1058 (m), 1027 (m), 796 (m), 703 (m), 636 (w), 615 (w).

$[(OH_2)(MeO\text{-terpy})Mn(\mu\text{-}O)_2Mn(MeO\text{-terpy})(OH_2)](NO_3)_3$ (1MeO-$(NO_3)_3$). **1MeO**$(NO_3)_3$ was prepared similarly to **1MeS**$(NO_3)_3$ using MeO-terpy (45.3 mg, 0.172 mmol). Yield: 43.9 mg (59.3%). Anal. $C_{34}H_{35}Mn_2N_9O_{15.5}$, **1MeO**$(NO_3)_3{\cdot}0.5H_2O$, Calcd: C 42.73%, H 3.47%, N 14.01%. Found: C 42.51%, H 3.27%, N 14.02%. UV−vis spectrum (H_2O): λ_{max} (ε) = 552 (619), 655 (603 M^{-1} cm^{-1}). IR in cm^{-1} (KBr): ν = 3420 (m), 3066 (w), 1613 (s), 1570 (m), 1557 (m), 1483 (s), 1384 (s), 1229 (s), 1058 (m), 1034 (s), 795 (m), 703 (w), 638 (w), 613 (w).

$[(OH_2)(BuO\text{-terpy})Mn(\mu\text{-}O)_2Mn(BuO\text{-terpy})(OH_2)](NO_3)_3$ (1BuO-$(NO_3)_3$). **1BuO**$(NO_3)_3$ was prepared similarly to **1MeS**$(NO_3)_3$ using BuO-terpy (52.5 mg, 0.172 mmol). However, 1 mL of hot acetone was used as solvent to dissolve BuO-terpy. Yield: 42.4 mg (50.6%). Anal. $C_{38}H_{43}Mn_2N_9O_{15.5}$, **1BuO**$(NO_3)_3{\cdot}0.5H_2O$, Calcd: C 46.40%, H 4.41%, N 12.82%. Found: C 46.27%, H 4.17%, N 12.81%. UV−vis spectrum (H_2O): λ_{max} (ε) = 551 (623), 650 (610 M^{-1} cm^{-1}). IR in cm^{-1} (KBr): ν = 3412 (m), 3064 (w), 2957 (w), 2871 (w), 1613 (s), 1557 (m), 1480 (m), 1440 (m), 1385 (s), 1223 (s), 1163 (m), 1056 (m), 1028 (m), 797 (m), 704 (m), 635 (w), 616 (w).

$[(OH_2)(Cl\text{-terpy})Mn(\mu\text{-}O)_2Mn(Cl\text{-terpy})(OH_2)](NO_3)_3$ (1Cl$(NO_3)_3$). **1Cl**$(NO_3)_3$ was prepared as described in the literature.[31] Yield: 67.0%. UV−vis spectrum (H_2O): λ_{max} (ε) = 552 (610), 658 (603 M^{-1} cm^{-1}). IR in cm^{-1} (KBr): ν = 3403 (w), 3062 (m), 1597 (s), 1556 (m),

dx.doi.org/10.1021/ic201797h | Inorg. Chem. 2012, 51, 1530−1539

1479 (s), 1422 (m), 1384 (s), 1302 (m), 1023 (m), 831 (m), 795 (m), 712 (m), 639 (w), 612 (w).

Derivatives/Mica Adsorbates. An aqueous solution (~3 mM, 10 mL, pH = 4.0) of **1** derivatives was added to an aqueous suspension (5−15 mL, pH = 4.0) of mica (50−150 mg) to adsorb **1** derivatives onto mica from the solution. The suspension was filtered after stirring for 30 min, and then dried under vacuum to yield **1** derivatives/mica adsorbates. The amount (n_{ads}/mol) of **1** derivatives adsorbed was measured by the UV−vis absorption spectral change of the aqueous solution before and after adding mica.

Measurements. The UV−vis absorption spectra were measured in a quartz cell using a photodiode array spectrophotometer (Shimadzu, Multispec-1500). Infrared spectra were recorded with FTIR spectrometer (Shimadzu, FTIR-4200) as KBr pellets. The electrochemical measurement was performed in a 0.1 M KNO_3 aqueous solution (pH = 3.5) containing 0.1 mM **1** derivatives in a conventional single-compartment cell equipped with a glassy carbon electrode (effective area, 0.071 cm^2), a saturated calomel reference electrode (SCE), and a platinum wire counter electrode at 25 °C under an Ar atmosphere using an electrochemical analyzer (Hokuto Denko, HZ-3000). The cyclic voltammograms (CVs) were recorded at 20 mV s^{-1} of a scan rate. The differential pulse voltammograms (DPVs) were measured under the following conditions: pulse amplitude (E_{step}), 50 mV; sample width, 1 ms; pulse width, 5 ms; pulse period, 250 ms; scan rate, 5 mV s^{-1}. All crystals for X-ray diffraction measurement were mounted on a glass fiber. X-ray diffraction data were recorded on a Rigaku RAXIS-IV imaging plate diffractometer using the ω scan technique to a maximum 2θ value of 55.0° with graphite-monochromated Mn Kα (λ = 0.7107 Å) radiation at 23 °C. The structure was solved by heavy-atom Patterson methods and expanded using Fourier techniques. The non-hydrogen atoms were refined anisotropically. Hydrogen atom were included but not refined. The final cycle of full-matrix least-squares refinement was based on the observed reflections ($I > 2.00\sigma(I)$) and variable parameters and converged with unweighted and weighted agreement factor R and R_w. The magnetic susceptibilities of powdered **1** derivatives were measured by a superconducting quantum interference device (SQUID) with Quantum Design model MPMS7 in a temperature range 2−300 K and the magnetic field strength 5000 G. The experimental data were analyzed by nonlinear least-squares calculation performed by Igor Pro (Version 6.0.3.0, WaveMetrics Inc.). The heterogeneous water oxidation experiments were performed in the aqueous suspension containing 40 mg of the **1** derivatives/mica adsorbates (n_{ads} = 12.5−75 μmol g^{-1}) using a large excess (50 mM) of a Ce^{IV} oxidant (2.0 mL of a liquid phase volume, pH = 1.0 adjusted with HNO_3, 25 °C). The amount of O_2 evolved was analyzed using a Clark type O_2 analyzer (Hansatech Instruments, Oxygraph OXYG1 and DW1/AD unit). The long time-scale experiments (4 days) of water oxidation for turnover number calculations used a large reaction vial (25 mL), and the amount of O_2 evolved in headspace was analyzed using a gas chromatograph (Shimadzu, GC-8A) equipped with a molecular sieve 5 Å column using argon carrier gas (flow rate = 40 cm^3 min^{-1}) at 50 °C.

RESULTS

Synthesis, UV−Vis, and IR Spectroscopic Measurement. The synthesis of **1** derivatives by Chen et al. was conducted in a water−acetonitrile mixture solvent. As in our preliminary test, most derivatives of **1** were not very stable in a water−acetonitrile mixture solvent; we tried to synthesize **1** derivatives in an aqueous media. When the solubility of R-terpy in water is low, appropriate quantities of acetone were added in the aqueous solution. A series of **1** derivatives shown in Chart 1 were isolated by reactions of $Mn(NO_3)_2$ with $KMnO_4$ in the presence of R-terpy derivatives in an aqueous solution. The isolated yields were 44% (**1Me**$(NO_3)_3$)−89% (**1**$(NO_3)_3$). The relatively low yield of **1Me**$(NO_3)_3$ is due to its high solubility in water which makes it difficult to be isolated. **1Cl** is unstable in water at room temperature. However, the yield of **1Cl**$(NO_3)_3$ increased from 6.0% to 67.0% by employing the low temperature and dark conditions.[31] The UV−vis and IR absorption spectroscopic data are summarized in Table 1. (UV−vis absorption spectra shown in Figures S1 and S2). All the isolated **1** derivatives in water exhibited nearly the same UV−vis absorption spectra in a visible region, giving the characteristic absorption at 551−552 nm (ε = 605−623 M^{-1} cm^{-1}) and 650−658 nm (ε = 598−610 M^{-1} cm^{-1}) that are assigned to a d−d transition and an O-to-Mn charge-transfer band based on the mixed-valence $Mn^{III}(\mu\text{-}O)_2Mn^{IV}$ core, respectively.[38−40] For comparison, the λ_{max} values for the d−d transition are close to those (525 and 555 nm) for the well-defined $[(bpy)_2Mn(\mu\text{-}O)_2Mn(bpy)_2]^{3+}$ and $[(phen)_2Mn(\mu\text{-}O)_2Mn(phen)_2]^{3+}$ (phen = 1,10-phenanthroline) dimers, but λ_{max} values for the O-to-Mn charge-transfer transition are shorter than those (684 nm) for the reference dimers. In IR spectra, the peak around 700 cm^{-1} was assigned to asymmetric stretch (ν_{as}) on a Mn−O−Mn bond according to the literature.[40] The ν_{as} energy are 698−705 cm^{-1} for most derivatives, but high (712 cm^{-1}) for **1Cl**.

Table 1. Summary of UV−Vis and IR Data

	UV−vis data				IR data
	d−d transition		O-to-Mn charge transfer		Mn−O−Mn bond
complexes	λ_{max}/nm	ε/M^{-1} cm^{-1}	λ_{max}/nm	ε/M^{-1} cm^{-1}	ν_{as}/cm^{-1}
1Cl[31]	552	610	658	603	712
1	551	605	655	600	698
1MeS	552	616	655	604	700
1Me	551	619	655	608	702
1EtO	552	620	655	598	705
1PrO	552	610	655	603	703
1MeO	552	619	655	603	703
1BuO	551	623	650	610	704
1[38]	553	678	654	585	703
$[(bpy)_2Mn^{III}(\mu\text{-}O)_2Mn^{IV}(bpy)_2]^{3+}$[40]	525 555	530 455	684	561	688
$[(phen)_2Mn^{III}(\mu\text{-}O)_2Mn^{IV}(phen)_2]^{3+}$[40]	525 555	509 427	684	553	686

X-ray Diffraction Crystallographic Structures of 1 Derivatives. The X-ray diffraction crystallographic data are summarized in Table 2, and the selected bond lengths, angles, and torsion angles related to the $Mn(\mu\text{-}O)_2Mn$ core for each derivative are shown in Table 3. For all the derivatives, the Mn−O_μ (O_μ: μ-bridging oxygen atom) bond lengths (1.769−1.859 Å) are shorter than the Mn−O_t (O_t: oxygen atom of terminal aquo ligands) bond lengths (2.005−2.043 Å), and the Mn···Mn distances lie in the range 2.707−2.753 Å. Although all the derivatives contain the formally mixed valence $Mn^{III}(\mu\text{-}O)_2Mn^{IV}$ cores, the structure of the core gives two separate types of geometry. This is illustrated by the ORTEP diagrams of **1MeS** and **1MeO** shown in Figure 1A,B, respectively. The averaged Mn−O_μ bond length is the same as the Mn*−O_μ bond length of the other Mn center for **1MeS** (Figure 1A, Chart 2, and Table 4). This indicates that two Mn centers in the core for **1MeS** are crystallographically indistinguishable. Moreover, the terminal aquo ligands lie in the $Mn(\mu\text{-}O)_2Mn$ core planar for **1MeS** (O(2)−Mn−Mn-O(1)′ torsion angle[41] = 178.5°, see Table 3), as displayed by the Mercury view of the core from the Mn−Mn axis in a lower part of Figure 1A. The similar core geometries

dx.doi.org/10.1021/ic201797h | Inorg. Chem. 2012, 51, 1530−1539

Table 2. X-ray Crystallographic Data

	1EtO$(NO_3)_3{\cdot}2.5H_2O$	**1PrO**$(NO_3)_3{\cdot}3.5H_2O$	**1MeO**$(NO_3)_3{\cdot}3H_2O$	**1BuO**$(NO_3)_3{\cdot}4H_2O$	**1MeS**$(NO_3)_3{\cdot}6H_2O$	**1Me**·2[Mn(Me-terpy)$(NO_3)(H_2O)_2$]$(NO_3)_5{\cdot}6H_2O$
empirical formula	$Mn_2O_{17.50}N_9C_{34}H_{39}$	$Mn_2O_{18.50}N_9C_{36}H_{45}$	$Mn_2O_{18}N_9C_{32}H_{36}$	$Mn_2O_{19}N_9C_{38}H_{50}$	$Mn_2S_2O_{19}N_9C_{32}H_{42}$	$Mn_4O_{35}N_{19}C_{64}H_{76}$
fw	963.61	1009.68	944.56	1046.74	1030.73	1891.16
cryst syst	triclinic	triclinic	monoclinic	triclinic	triclinic	triclinic
space group	$P\bar{1}$ (No. 2)	$P\bar{1}$ (No. 2)	$P2_1/c$ (No. 14)	$P\bar{1}$ (No. 2)	$P\bar{1}$ (No. 2)	$P\bar{1}$ (No. 2)
a, Å	9.0452(8)	11.6339(1)	10.587(1)	9.3943(2)	9.9219(8)	7.8030(2)
b, c	11.2717(3)	13.5458(1)	16.337(2)	11.7585(6)	10.668(1)	14.1073(4)
c, Å	11.6197(2)	15.7383(3)	22.822(3)	11.7303(6)	11.1863(8)	18.5840(6)
α, deg	71.876(4)	102.065(1)		77.790(1)	64.322(5)	84.391(2)
β, deg	66.648(9)	98.554(1)	98.267(2)	82.7795(9)	83.790(6)	83.461(3)
γ, deg	78.008(7)	110.9125(9)		66.296(4)	80.843(2)	84.560(2)
V, Å^3	1028.8(1)	2196.89(6)	3906.1(8)	1158.41	1052.5(2)	2015.4(1)
Z	1	2	4	1	1	1
T, °C	23	23	23	23	23	23
λ, Å	0.71069	0.71069	0.71069	0.71069	0.71069	0.71069
d_{calcd}, g/cm^3	1.555	1.526	1.606	1.500	1.626	1.558
F_{000}	496.00	1044.00	1940.00	543.00	531.00	973.00
no. reflns total/unique	7918/4382	17 767/9377	10 862/6104	6337/3889	7316/4335	15 637/8498
no. obsd ($I > 2.00\sigma(I)$)	4382	9377	6104	3889	4335	8498
reflns/params ratio	11.12	15.27	11.08	11.21	13.72	13.86
R; R_w	0.093;[a] 0.152[b]	0.094;[a] 0.174[b]	0.140;[a] 0.192[b]	0.107;[a] 0.221[b]	0.106;[a] 0.145[b]	0.105;[a] 0.194[b]
GOF indicator	1.2	1.28	1.44	1.27	1.22	1.20

[a] $R = \sum(F_o^2 - F_c^2)/\sum F_o^2$. [b] $R_w = [\sum w(F_o^2 - F_c^2)^2/\sum w(F_o^2)^2]^{1/2}$.

were observed for **1Me**, **1EtO**, and **1BuO** derivatives, as well as **1**[21] reported earlier.

For **1MeO** (Figure 1B), the averaged Mn−O_μ bond (1.780 and 1.841 Å) is different from the Mn*−O_μ bond by 0.061 Å, showing that two Mn centers in the cores are crystallographically distinguishable in contrast to the indistinguishable Mn centers of **1MeS** (Chart 2 and Table 4). The Mn* center with the longer Mn*−O bond can be assigned to a Mn^{III} ion, with the other center being assigned to a Mn^{IV} ion. This assignment is supported by the different geometries around Mn ions related to a Jahn−Teller distortion. For **1MeO**, the Mn* center is typical of an axially elongated d^4 Mn^{III} ion, in which the averaged Mn*−N_{ax} bond (2.245 Å, N_{ax}: nitrogen atom of an axial configuration) is longer than the Mn*−N_{eq} bond (2.105(5) Å, N_{eq}: nitrogen atom of an equatorial configuration) by 0.140 Å (Chart 2 and Table 4). The difference in the bond length (0.140 Å) is significantly longer than the corresponding difference (0.058 Å) between the Mn−N_{ax} (2.061 A) and Mn−N_{eq} (2.003 A) bonds. The Mercury view (lower in Figure 1B) of the core from the Mn−Mn axis for **1MeO** shows that one of the terminal aquo ligands is significantly deviated from the core plane (O(4)−Mn(2)−Mn(1)−O(2) torsion angle = 170.74°, see Table 3), in contrast to the geometry with the terminal aquo ligands lying in the core plane for **1MeS**. Likewise, for **1PrO** and **1MS**,[33] the crystallographically distinguishable Mn centers in the core were also observed (the differences (ΔMn−O_μ) between the averaged Mn−O_μ and Mn*−O_μ bonds are 0.059 and 0.037 Å[33] for **1PrO** and **1MS**, respectively), and one of the terminal aquo ligands is deviated from the core plane.

Magnetic Susceptibility Measurement. The magnetic susceptibilities (χ_{mol}/cm^3 mol^{-1}) of derivatives were measured in the range 2−300 K. The effective magnetic moment (μ_{eff}) per mol decreased with a lowering of temperature and converged on the range of 1.79 μ_B (μ_B is the Bohr magneton) at 100 K although it increased slightly below 100 K for derivatives used (Figure 2 for **1EtO**). This converged value is close to $\sqrt{3}$ μ_B expected for the spin-only moment of a Mn^{III}−Mn^{IV} dimer with antiferromagnetic coupling, supporting the $Mn^{III}(\mu\text{-}O)_2Mn^{IV}$ core of the derivatives. The χ_{mol} data were analyzed using eq 1 derived from the isotropic Heisenberg exchange Hamiltonian $H = -2JS_1{\cdot}S_2$

$$\chi_{mol} = \frac{Ng^2\beta^2}{3kT}\frac{\sum_{S_T} S_T(S_T+1)(2S_T+1)\exp(JS_T(S_T+1)/kT)}{\sum_{S_T}(2S_T+1)\exp(JS_T(S_T+1)/kT)} + K + \frac{C}{T} \quad (1)$$

where S_T (the total spin quantum number) assumes the values of $^7/_2$, $^5/_2$, $^3/_2$, and $^1/_2$ for the $S_1 = 2$, $S_2 = {}^3/_2$ system, *g* is Lande's *g* factor, *J* is the exchange integral, *K* accounts for temperature-independent paramagnetism and small correction to the diamagnetic contribution, and *C*/*T* accounts for the paramagnetic impurities; *N*, *β*, and *k* are Avogadro's number, the Bohr magneton, and Boltzmann's constant, respectively. The best fit to χ_{mol} data was given by the following parameters: $J = -186$ cm^{-1}, $g = 2.00$, $K = 2.3 \times 10^{-3}$ cm^3 mol^{-1}, $C = 3.1 \times 10^{-2}$ cm^3 K mol^{-1} for **1EtO**. The *C* value indicates the low paramagnetic impurities (approximately 0.8%) by Mn^{II} ions and assures high purity of 99.2% of the sample. The parameters given for the best fitting are summarized in Table 5. The *C* value assures high purity (99.97−98.8%) of the derivative samples used. The *g* values are close to 2.0 for all the derivatives, which is consistent with previously reported $Mn^{III}(\mu\text{-}O)_2Mn^{IV}$ dimer complexes.[42−44] All the *J* values ($J = -196$ to -161 cm^{-1}) given are negative, indicating antiferromagnetic interaction between the Mn centers, as seen for the previously reported dimers.[42−50]

dx.doi.org/10.1021/ic201797h | Inorg. Chem. 2012, 51, 1530−1539

Table 3. Selected Bond Lengths [Å], Angles [deg], and Torsion Angles [deg]

1MeS[a]			
Mn−N(1)	2.025(2)	Mn−N(2)	2.133(3)
Mn−N(3)	2.129(2)	Mn−O(1)	1.803(2)
Mn−O(1)′	1.822(2)	Mn−O(2)	2.043(2)
Mn−Mn	2.7183(8)		
Mn−O−Mn	97.17(9)	O(1)−Mn−O(1)′	82.83(9)
O(2)−Mn−Mn−O(1)	178.5	O(2)−Mn−Mn−O(1)′	178.5
1Me[a]			
Mn−N(1)	2.046(3)	Mn−N(2)	2.139(3)
Mn−N(3)	2.146(3)	Mn−O(1)	1.817(2)
Mn−O(1)′	1.820(2)	Mn−O(2)	2.004(2)
Mn−Mn	2.753(1)		
Mn−O−Mn	98.4(1)	O(1)−Mn−O(1)′	81.6(1)
O(2)−Mn−Mn−O(1)	179.8	O(2)−Mn−Mn−O(1)′	179.8
1EtO[a]			
Mn−N(1)	2.024(3)	Mn−N(2)	2.121(4)
Mn−N(3)	2.130(3)	Mn−O(1)	1.791(3)
Mn−O(1)′	1.810(2)	Mn−O(2)	2.015(3)
Mn−Mn	2.707(1)		
Mn−O−Mn	97.5(1)	O(1)−Mn−O(1)′	82.5(1)
O(2)−Mn−Mn−O(1)	179.2	O(2)−Mn−Mn−O(1)′	179.2
1PrO[b]			
Mn(1)−N(1)	1.984(3)	Mn(1)−N(2)	2.033(3)
Mn(1)−N(3)	2.038(3)	Mn(1)−O(1)	1.789(3)
Mn(1)−O(2)	1.787(2)	Mn(1)−O(3)	2.009(3)
Mn(2)−N(4)	2.081(3)	Mn(2)−N(5)	2.255(3)
Mn(2)−N(6)	2.247(3)	Mn(2)−O(1)	1.837(2)
Mn(2)−O(2)	1.859(3)	Mn(2)−O(4)	2.020(3)
Mn(1)−Mn(2)	2.7391(7)		
Mn(1)−O(1)−Mn(2)	98.1(1)	Mn(1)−O(2)−Mn(2)	97.3(1)
O(1)−Mn(1)−O(2)	83.9(1)	O(1)−Mn(2)−O(2)	80.6(1)
O(3)−Mn(1)−Mn(2)−O(1)	178.6	O(4)−Mn(2)−Mn(1)−O(1)	175.5
O(3)−Mn(1)−Mn(2)−O(2)	179.6	O(4)−Mn(2)−Mn(1)−O(2)	174.5
1MeO[b]			
Mn(1)−N(1)	2.003(5)	Mn(1)−N(2)	2.057
Mn(1)−N(3)	2.065(5)	Mn(1)−O(1)	1.769
Mn(1)−O(2)	1.791(4)	Mn(1)−O(3)	2.010
Mn(2)−N(4)	2.105(5)	Mn(2)−N(5)	2.245
Mn(2)−N(6)	2.245(5)	Mn(2)−O(1)	1.830
Mn(2)−O(2)	1.850(4)	Mn(2)−O(4)	2.014
Mn(1)−Mn(2)	2.726(1)		
Mn(1)−O(1)−Mn(2)	98.5(2)	Mn(1)−O(2)−Mn(2)	97.0(2)
O(1)−Mn(1)−O(2)	84.0(2)	O(1)−Mn(2)−O(2)	80.6(2)
O(3)−Mn(1)−Mn(2)−O(1)	174.2	O(4)−Mn(2)−Mn(1)−O(1)	172.84
O(3)−Mn(1)−Mn(2)−O(2)	176.3	O(4)−Mn(2)−Mn(1)−O(2)	170.74
1BuO[a]			
Mn−N(1)	2.042(3)	Mn−N(2)	2.128(4)
Mn−N(3)	2.145(4)	Mn−O(1)	1.825(3)
Mn−O(1)′	1.811(3)	Mn−O(2)	2.018(3)
Mn−Mn	2.741(1)		
Mn−O−Mn	97.8(1)	O(1)−Mn−O(1)′	82.2(1)
O(2)−Mn−Mn−O(1)	178.9	O(2)−Mn−Mn−O(1)′	178.9

[a]Label numbers on atoms are according to those of **1MeS** in Figure 1A. [b]Label numbers on atoms are according to those of **1MeO** in Figure 1B.

Electrochemical Measurement. The CV of **1** in an aqueous 0.1 M KNO_3 solution (black line in Figure 3) gave an anodic peak (P_a^1) at 1.00 V vs SCE, assigned to the oxidation of Mn^{III}−Mn^{IV} to Mn^{IV}−Mn^{IV}. Three cathodic peaks (P_c^1, P_c^2, and P_c^3) were also observed at 0.92, 0.80, and 0.62 V, assigned to reductions of (1) Mn^{IV}−Mn^{IV} to Mn^{III}−Mn^{IV}, (2) tetranuclear Mn^{IV}_4 species[51] formed from the Mn^{IV}−Mn^{IV} dimer to the Mn^{III}−Mn^{IV} dimer, and (3) Mn^{III}−Mn^{IV} to the Mn^{II} monomer, respectively. These assignments are well-defined in the literature.[52] The CV of **1EtO** exhibited the corresponding anodic response of P_a^1 and cathodic responses of P_c^1, P_c^2, and P_c^3. These redox responses shifted to the lower potentials compared with those for **1** due to electron-donating ability of the 4′-substituted EtO groups. Although the CVs of the other derivatives were measured under the same conditions, the clear redox responses were not given for **1Me** and **1Cl** (except P_c^3 for **1Cl**). The CV of **1MeS** could not be taken under the conditions employed because it is unstable in concentrated electrolyte solutions. To reveal the substituent effect on the redox properties of the derivatives, the redox potentials of the Mn^{III}−Mn^{IV}/Mn^{IV}−Mn^{IV} pair around 1.0 V were carefully measured using a differential pulse voltammetry (DPV) technique. DPV data for **1** and **1EtO** are displayed in the inset of Figure 3, in which the clear anodic waves due to the Mn^{III}−Mn^{IV}/Mn^{IV}−Mn^{IV} pair were given at 0.927 and 0.899 V as the peak potential (E_p), respectively. Similarly, the clear anodic peaks were successfully observed for **1Me** and **1Cl**. The half wave potentials ($E_{1/2}$) were calculated according to $E_{1/2} = E_p + E_{step}$ and given as averaged values of 10−15 times DPV measurements to be summarized in Table 6 together with CV data.

Preparation and Characterization of 1 Derivatives/Mica Adsorbates. The **1** derivatives were adsorbed onto mica in aqueous suspension by cation exchange with Na^+. The adsorption isotherm of each derivative onto mica was almost identical to that of **1** reported earlier,[20] showing that the adsorption aspects of the derivatives are not influenced to great extent by the 4′-substituent variation employed. The maximum concentrations of the derivatives adsorbed on mica are 0.41 ± 0.02 mmol g^{-1} for all derivatives. These are nearly one-third of CEC (1.2 eq mmol g^{-1}) of mica, indicating that all the derivatives are adsorbed on mica with trivalence of the cation kept. Compound **1** adsorbed on mica was earlier characterized by the UV−vis diffuse reflectance and Mn K-edge X-ray absorption near edge structure spectroscopic measurement.[20]

An XRD spectroscopic technique was used to evaluate the influence of the bulky substituents on the interlayer space of the derivatives/mica adsorbates. Figure 4 shows the XRD patterns of mica adsorbates with **1**, **1EtO**, **1PrO**, and **1BuO**. The XRD patterns of neat mica gave an intense peak at 2θ = 7.18° (interlayer distance of 12.3 Å). These XRD patterns for derivatives/mica adsorbates exhibited a slightly broad peak around 2θ = 6.98−7.14°, corresponding to 12.65−12.37 Å of the interlayer distance. The interspace distance between the layers can be given as 6.05−5.77 Å from the interlayer distance (12.65−12.37 Å) and the layer thickness (6.6 Å). The difference in the interspace distance among the adsorbates used is at most 0.28 Å (4.8%), showing that the influence of the 4′-substituent variation on the interspace distance is negligible.

Water Oxidation Catalysis by 1 Derivatives/Mica Adsorbates and Kinetic Analysis. In the reaction of the **1**/mica adsorbate with a Ce^{IV} oxidant in water, the **1**/mica adsorbate catalyzed water oxidation to evolve O_2. This is illustrated by the time course (red plots) of the amount (n_{O2}/mol) of O_2 evolved in the reaction (Figure 5). The time course of n_{O2} using the **1EtO**/mica adsorbate is shown by blue plots in

dx.doi.org/10.1021/ic201797h | Inorg. Chem. 2012, 51, 1530−1539

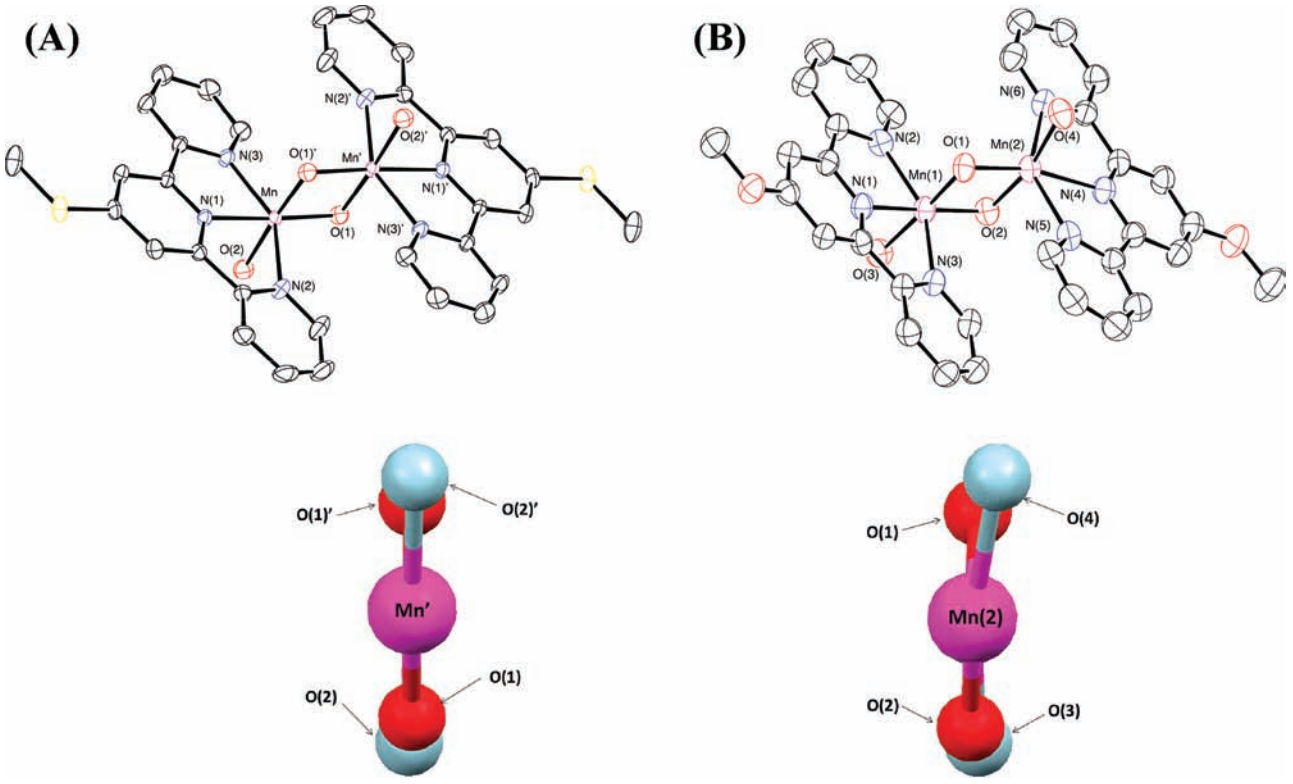

Figure 1. ORTEP views of (A) **1MeS** and (B) **1MeO** with 30% of thermal ellipsoids (upper) and Mercury views (bottom) of the Mn(μ-O)$_2$Mn core with terminal aquo ligands from the Mn−Mn axis. The labeled atoms are according to those in Chart 2.

Chart 2. Labeled Atoms and Core Geometry around Mn Centers for Table 4[a]

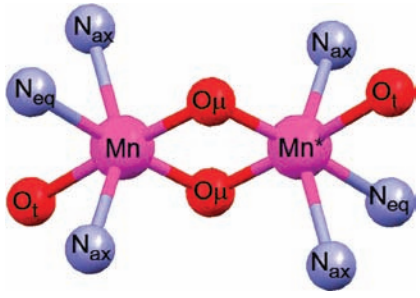

[a] O$_\mu$, μ-bridging oxygen atom; O$_t$, oxygen atom of terminal aquo ligands; N$_{eq}$, nitrogen atoms of an equatorial configuration; N$_{ax}$, nitrogen atoms of an axial configuration.

Figure 5. The n_{O2} (9 nmol) in 20 min for the **1EtO**/mica adsorbate was 52 times lower than that (471 nmol) for the **1**/mica adsorbate under the same conditions due to the loading of EtO groups. The initial O_2 evolution rate (v_{O2}/mol s^{-1}) was calculated from the initial slope of the time course of n_{O2}. The plots of v_{O2} versus n_{ads} gave an upward curve for each derivative (Figure 6). The v_{O2} data were analyzed by the kinetic model (eq 2) assuming a combination between first and second order O_2 evolutions with respect to the adsorbed derivative

$$v_{O2} = k_1 n_{ads} + k_2 n_{ads}^{\ 2} \quad (2)$$

where k_1/s^{-1} and k_2/mol^{-1} s^{-1} are the first order and second order rate constants for O_2 evolution, respectively. For comparing the turnover frequency of each derivative adsorbed, v_{O2} was normalized by n_{ads} to define the apparent turnover frequency, k_{app}/s^{-1}, as eq 3. The linear plots of k_{app} versus n_{ads} can provide k_1 and k_2 from the intercept and the slope, respectively.

$$k_{app} = v_{O2}/n_{ads} = k_1 + k_2 n_{ads} \quad (3)$$

The plots of k_{app} versus n_{ads} in Figure 7 gave a straight line with the significant slope passing through the very near origin for **1**, **1Me**, **1EtO**, and **1MeO** to give k_2 values and k_1 of nearly zero, suggesting that O_2 is predominantly evolved by a bimolecular reaction of the derivatives.[19] It was interpreted by the cooperative catalysis involving 2 equiv of derivatives.[19] The linear plots of k_{app} versus n_{ads} for **1MeS** and **1PrO** gave the significant intercepts to give k_1 values. It suggests that the unimolecular O_2 evolution reaction competes with the bimolecular reaction for **1MeS** and **1PrO**. The k_1 and k_2 values for these derivatives are summarized in Table 7 including those of **1** and **1Cl** reported earlier. For **1Cl** giving $k_1 = 6.8 \times 10^{-5}$ s^{-1} and k_2 of nearly zero, it was suggested that O_2 evolution shows first order kinetics with respect to **1Cl** adsorbed. The first order kinetics was explained by noncatalytic O_2 evolution involved in the unimolecular decomposition of **1Cl**.[31] This is consistent with the maximum turnover number (TN = 0.52) of **1Cl** that is less than unity (Table 7). The first order reaction of **1MeS** and **1PrO** could also be explained by noncatalytic O_2 evolution involved in the unimolecular decomposition.

DISCUSSION

Substituent Effect on the Geometrical and Electric Structures of the Mn(μ-O)$_2$Mn Cores. The UV−vis spectra data suggested that the electronic structure of the Mn^{III}(μ-O)$_2$Mn^{IV} core is hardly influenced by 4′-substituent variation that we have employed. However, IR data showed that the Mn−O−Mn bond in the core is significantly strengthened by

dx.doi.org/10.1021/ic201797h | Inorg. Chem. 2012, 51, 1530−1539

Table 4. Summary of the Selected Bond Lengths around Mn−Oxo centers in the $Mn^{III}(\mu\text{-}O)_2Mn^{IV}$ Core[a]

complex	Mn−Mn*	Mn−O_μ[b]	Mn*−O_μ[b]	Δ(Mn−O_μ)[c]	Mn−N_{ax}	Mn−N_{eq}[b]	Δ(Mn−N)[d]	Mn*−N_{ax}	Mn*−N_{eq}[b]	Δ(Mn*−N)[e]	Δ(Δ(Mn−N))[f]
1[21]	2.733(3)	1.810	1.810	0	2.117	2.044(8)	0.072	2.117	2.044(8)	0.072	0.000
1MeS	2.7183(8)	1.813	1.813	0	2.131	2.025(2)	0.106	2.131	2.025(2)	0.106	0.000
1Me	2.753(1)	1.819	1.819	0	2.143	2.046(3)	0.097	2.143	2.046(3)	0.097	0.000
1EtO	2.707(1)	1.811	1.811	0	2.126	2.024(3)	0.102	2.126	2.024(3)	0.102	0.000
1PrO	2.7391(7)	1.789	1.848	0.059	2.036	1.984(3)	0.051	2.251	2.081(3)	0.170	0.118
1MeO	2.726(1)	1.780	1.841	0.061	2.061	2.003(5)	0.058	2.245	2.105(5)	0.140	0.082
1BuO	2.741(1)	1.818	1.818	0	2.137	2.042(3)	0.095	2.137	2.042(3)	0.095	0.000
1MS[33]	2.7204(13)	1.789	1.826	0.037	2.048	2.037(7)	0.011	2.207	2.054(7)	0.153	0.142

[a]The Mn* center was distinguished from the other Mn center. The Mn* and Mn centers are assigned to Mn^{III} and Mn^{IV} ions, respectively. [b]The bond length was calculated from the average of a pair of bond lengths. [c]Δ(Mn−O_μ) = (Mn*−O_μ) − (Mn−O_μ). [d]Δ(Mn−N) = (Mn−N_{ax}) − (Mn−N_{eq}). [e]Δ(Mn*−N) = (Mn*−N_{ax}) − (Mn*−N_{eq}). [f]Δ(Δ(Mn−N)) = Δ(Mn*−N) − Δ(Mn−N).

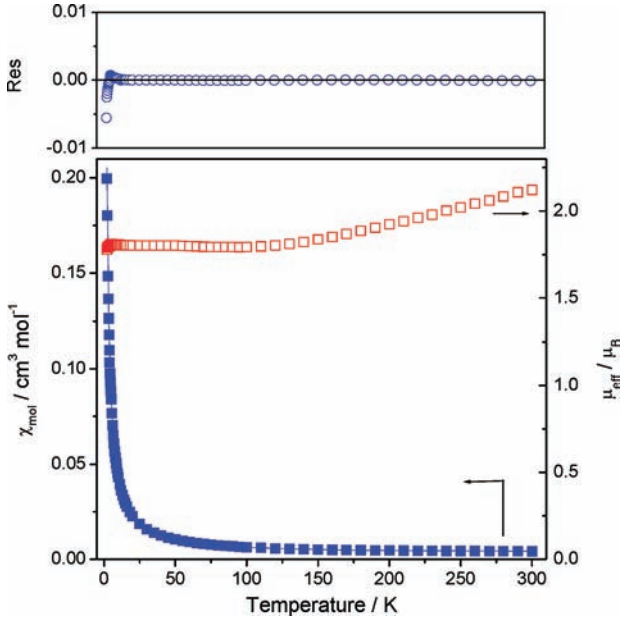

Figure 2. Temperature dependences of molar magnetic susceptibility (χ_{mol}) and effective magnetic moment (μ_{eff}) per mol for **1EtO**.

Table 5. Summary of Parameters for the Magnetic Susceptibility Analysis

complex	J/cm^{-1}	g	K/cm^3 mol^{-1}	C/cm^3 K mol^{-1}
1Cl	−196	2.09	1.0×10^{-3}	2.9×10^{-2}
1	−188	2.06	1.6×10^{-3}	2.1×10^{-2}
1EtO	−186	2.00	2.3×10^{-3}	3.1×10^{-2}
1MeS	−178	2.00	1.3×10^{-4}	1.1×10^{-2}
1PrO	−163	1.98	1.5×10^{-3}	4.7×10^{-2}
1MeO	−161	1.93	2.9×10^{-3}	1.0×10^{-2}

loading the electron-withdrawing Cl groups, though electron-donating MeO and EtO groups did not give such effect on strength of Mn−O−Mn bond. The ionic bonding property between the anionic O_μ bridges and cationic Mn center ions could be enhanced by the electron-withdrawing Cl groups. The lowest energy bands (650−658 nm) in UV−vis absorption spectra previously assigned to an O-to-Mn charge-transfer band[38−40] give the very low extinction coefficients that are similar values to those assigned to the higher energy d−d transition. These data may suggest that the lowest energy band does not have as much contribution from that transition in this derivative series.

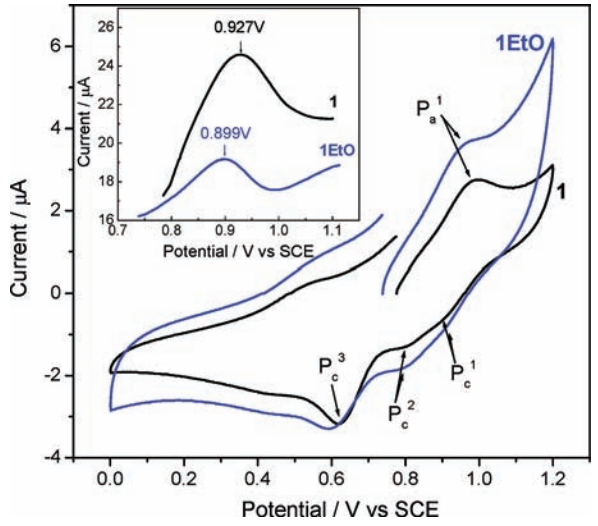

Figure 3. CVs of 0.1 mM **1** or **1EtO** in a 0.1 M KNO_3 aqueous solution at 20 mV s^{-1}. The inset is DPV data under the same conditions: pulse amplitude (E_{step}), 50 mV; sample width, 1 ms; pulse width, 5 ms; pulse period, 250 ms; scan rate, 5 mV s^{-1}.

X-ray crystallographic data displayed that the core geometry is changed by 4′-substituent variation; the Mn centers in the core are crystallographically indistinguishable for **1**,[21] **1MeS**, **1Me**, **1EtO**, and **1BuO** derivatives, but are significantly distinguishable for **1MeO**, **1PrO**, and **1MS**[33] (Table 4). The indistinguishable Mn centers could be caused by rapid electron exchange between the Mn centers to result in the delocalized $Mn(\mu\text{-}O)_2Mn$ core.[42] The delocalization could involve the terminal aquo ligands lying in the $Mn(\mu\text{-}O)_2Mn$ core plane. The electron donating ability of the 4′-substituted groups seems to induce the localized $Mn^{III}(\mu\text{-}O)_2Mn^{IV}$ core (Table 4), possibly by the slowing-down electron exchange. However, the mechanism of controlling the electron exchange between the Mn centers in the core remains unsolved in the present stage.

As for the redox properties, the $E_{1/2}$ value decreased in the order Cl > H > Me > EtO according to the electron-donating ability of the substituent groups (Hammett constants (σ_p) are shown in Table 6). However, the $E_{1/2}$ values of **1PrO**, **1MeO**, and **1BuO** deviated from this correlation between $E_{1/2}$ and σ_p. The localization of the core might be an important factor for their redox properties. (The cores of **1MeO** and **1PrO** are localized, *vide supra*.)

Substituent Effect on Magnetic Properties. The J value (−196 cm^{-1}) of **1Cl** is lower than that (−188 cm^{-1}) of **1** (Table 5), meaning that antiferromagnetic interaction between Mn centers for

dx.doi.org/10.1021/ic201797h | Inorg. Chem. 2012, 51, 1530−1539

Table 6. Summary of Electrochemical Data

		CV					DPV
		$Mn^{III}–Mn^{IV}/Mn^{IV}–Mn^{IV}$					
	σ_p[a]	E_{pa}	E_{pc}	$E_{1/2}$	$Mn^{III}–Mn^{IV}/Mn^{IV}_4$ E_{pc}	$Mn^{II}/Mn^{III}–Mn^{IV}$ E_{pc}	$Mn^{III}–Mn^{IV}/Mn^{IV}–Mn^{IV}$ $E_{1/2}$
1Cl	0.23					0.62	0.989
1	0	1.00	0.93	0.97	0.80	0.62	0.977
1Me	−0.17						0.959
1EtO	−0.24	0.96	0.92	0.94	0.80	0.59	0.949
1PrO	−0.25	0.98	0.95	0.97	0.80	0.60	0.972
1MeO	−0.27	0.99	0.92	0.96	0.79	0.58	0.964
1BuO	−0.32	1.00	0.94	0.97	0.78	0.58	0.969

[a]Hansch, C.; Leo, A.; Taft, R. W. *Chem. Rev.* **1991**, *91*, 165−195.

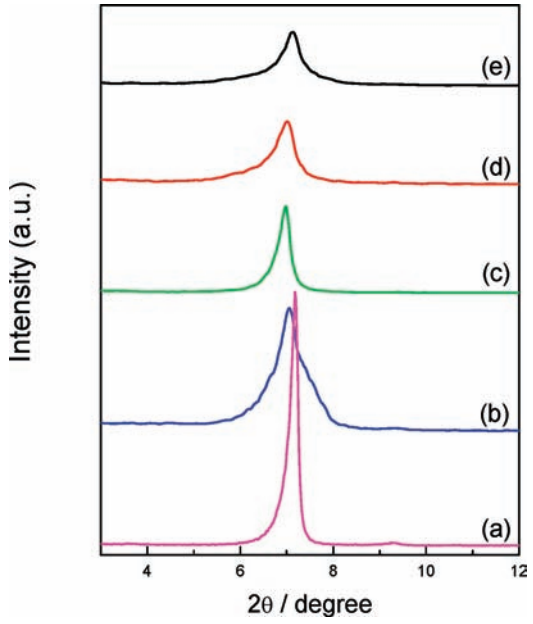

Figure 4. XRD patterns of derivatives/mica adsorbates (n_{ads} = 80 μmol g^{-1}): (a) neat mica, (b) **1**/mica, (c) **1EtO**/mica, (d) **1PrO**/mica, (e) **1BuO**/mica.

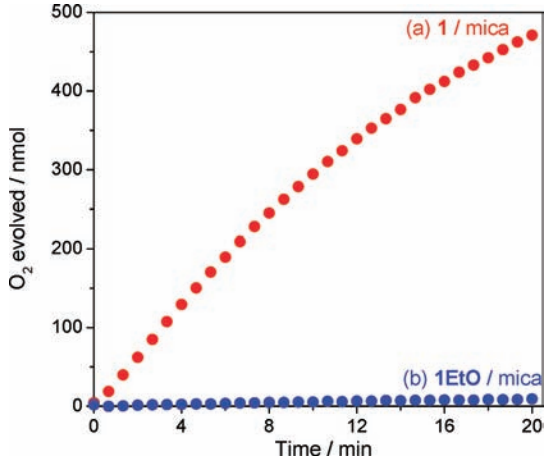

Figure 5. Time courses of the amount (n_{O2}/mol) of O_2 evolved in the reaction of aqueous suspention of the (a) **1**/mica adsorbate or (b) **1EtO**/mica adsorbate with a Ce^{IV} oxidant: 40 mg mica, 2.0 μmol **1** or **1EtO**, 100 μmol (50 mM) Ce^{IV}, 2 mL liquid volume, pH = 1.0.

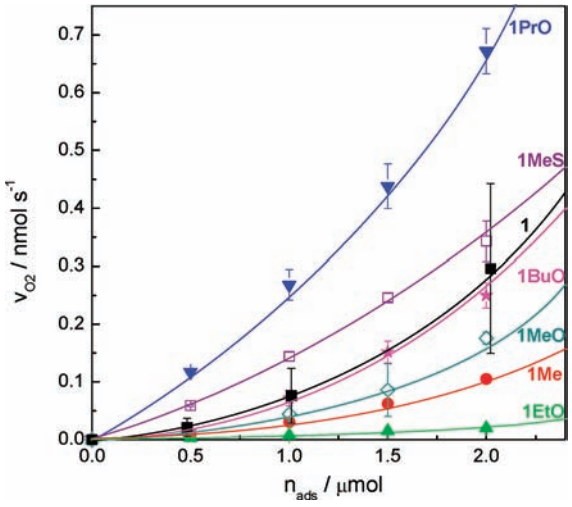

Figure 6. Plots of initial O_2 evolution rate (v_{O2}/mol s^{-1}) versus the amount (n_{ads}/mol) of derivatives adsorbed on mica: (■) **1**/ mica, (□) **1MeS**/mica, (●) **1Me**/mica, (▲) **1EtO**/mica, (◇) **1MeO**/mica, (▼) **1PrO**/mica, (★) **1BuO**/mica. The data of **1**/mica were cited from ref 20.

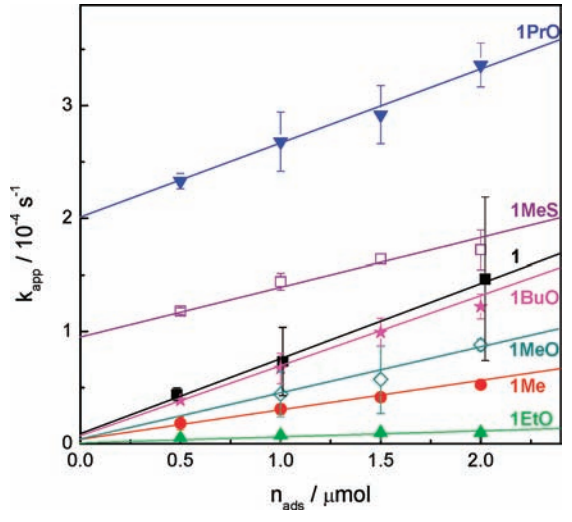

Figure 7. Plots of the apparent turnover frequency (k_{app}/s^{-1}) versus the amount (n_{ads}/mol) of derivatives adsorbed on mica: (■) **1**/ mica, (□) **1MeS**/mica, (●) **1Me**/mica, (▲) **1EtO**/mica, (◇) **1MeO**/mica, (▼) **1PrO**/mica, (★) **1BuO**/mica. The data of **1**/ mica were cited from ref 20.

1Cl is stronger than that for **1**. This could be due to the shorter Mn···Mn distance for **1Cl** than that for **1**. This is supported by the IR data showing that the ν_{as} energy of the Mn−O_μ bond for **1Cl** is higher than that of **1**. The J value (−188 cm^{-1}) of **1** is

dx.doi.org/10.1021/ic201797h | *Inorg. Chem.* 2012, 51, 1530−1539

Table 7. Summary of k_1, k_2 and the Maximum TN for Heterogeneous Water Oxidation

	k_1 (10^{-4} s^{-1})	k_2 (mol^{-1} s^{-1})	TN	ref
1Cl	0.68 (±0.02)	0[a]	0.52	31
1	0[a]	69 (±1.0)	15	20
1MeS	1.1 (±0.11)	36 (±8.0)	6.1	this work
1Me	0[a]	21 (±2.7)	6.4	this work
1EtO	0[a]	2.4 (±1.3)	4.1	this work
1PrO	2.1 (±0.12)	63 (±8.4)	13	this work
1MeO	0[a]	36 (±3.6)	7.3	this work
1BuO	0[a]	54 (±2.2)	10	this work

[a] k_1 and k_2 values (~ 0.1) were regarded as nearly zero because these values are lower than the maximum standard errors.

lower than those (−163 or −161 cm^{-1}) for **1PrO** or **1MeO** by 25 or 27 cm^{-1}, although the Mn···Mn distances are nearly the same among three derivatives (2.733(3), 2.7391(7), 2.726(1) Å for **1**, **1PrO**, and **1MeO**, respectively). A geometric study of $Mn^{IV}(\mu\text{-O})_2Mn^{IV}$ dimers and their correlation to magnetic properties were reported by Pecoraro's group.[53] There are good correlations between the J values and the Mn^{IV}–O_μ–Mn^{IV} angles or the Mn^{IV}···Mn^{IV} distances, but not between the Mn^{IV}–O_μ bond lengths or the pK_a values of the first protonation on the $Mn^{IV}(\mu\text{-O})_2Mn^{IV}$ cores. The J values of the **1** derivatives were plotted versus Mn^{III}–O_μ–Mn^{IV} angles or Mn^{III}···Mn^{IV} distances together with other values of previously reported $Mn^{III}(\mu\text{-O})_2Mn^{IV}$ dimers in Figures S3 and S4, respectively, but these plots did not give good correlations. This could be ascribed to the lessened planarity of $Mn^{III}(\mu\text{-O})_2Mn^{IV}$ cores (non-negligible dihedral angles, *vide supra*) compared with that of $Mn^{IV}(\mu\text{-O})_2Mn^{IV}$ cores, meaning that additional factors should be necessary to make a correlation between the J values and the geometrical structures.

Substituent Effect on Kinetics for Water Oxidation Catalysis. The k_2 values were highly variable from 2.4 to 69 mol^{-1} s^{-1} (Table 7). The k_2 value is responsible for the cooperative catalysis, which depends on the local concentration of the derivatives; the higher concentration is favorable for the cooperative catalysis.[19] There could be at least three possible explanations for the change of k_2 values. The first is a variation of the local concentration of the derivatives, which could be caused by the interlayer space change by the loaded bulky groups. However, this possibility could be excluded because XRD data show that the influence of the loaded substituent groups on the interspace distance between the mica layers is negligible (*vide supra*). The second is inhibition of cooperative catalysis by the steric hindrance of 4′-substituent groups. The second possibility could also be excluded because the k_2 values for **1PrO** and **1BuO** with more bulky substituent groups are remarkably higher than that for **1EtO**. The third is the intrinsic activity which is changed by the loading of substituent groups. To explore the third possibility, the k_2 values are plotted versus the σ_p value of substituent groups (Figure 8). The k_2 value decreased with a decrease of σ_p at a range of $-0.24 < \sigma_p < 0$, but deviated to an upper value from this correlation at $\sigma_p < -0.25$. It is notified that this σ_p profile of k_2 is similar to that of $E_{1/2}$ of a Mn^{III}–Mn^{IV}/Mn^{IV}–Mn^{IV} redox couple (*vide supra*). The significant correlation was provided between k_2 and $E_{1/2}$, as displayed in Figure 9. We are considering that the oxidation state of the active species for the catalysis is higher than Mn^{IV}–Mn^{IV}, being most likely Mn^{IV}–Mn^{V}. Assuming that the order of the oxidizing power of the active species on mica is consistent

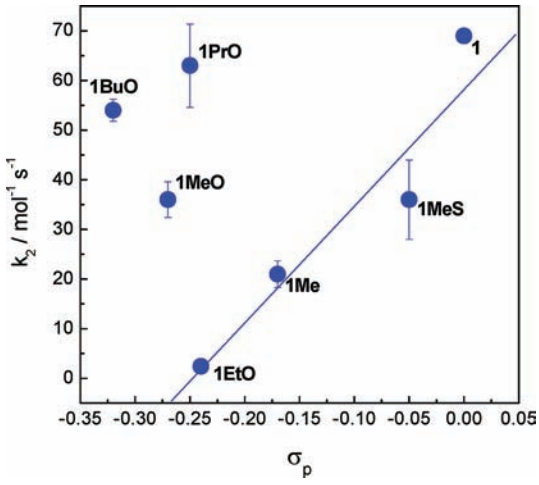

Figure 8. Relationship between the second order rate constant (k_2/mol s^{-1}) for O_2 evolution and Hammett constant (σ_p).

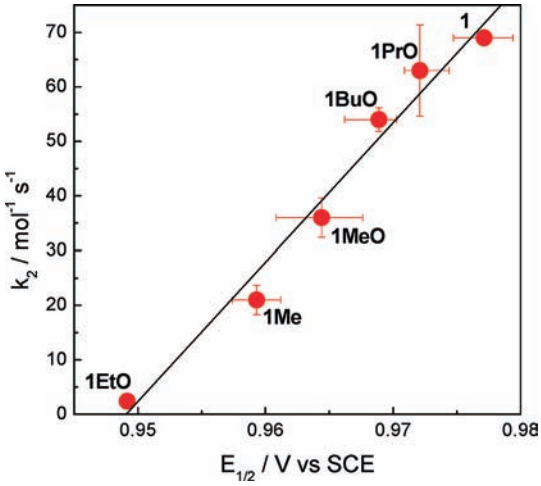

Figure 9. Relationship between the second order rate constant (k_2/mol s^{-1}) for O_2 evolution and half wave potential ($E_{1/2}$ vs SCE) of a Mn^{III}–Mn^{IV}/ Mn^{IV}–Mn^{IV} pair.

with the $E_{1/2}$ order (**1** > **1PrO** > **1BuO** > **1MeO** > **1Me** > **1EtO**) in solution, the k_2 increase might be interpreted by the increase of the oxidizing power. The linear correlation in Figure 9 shows that the k_2 value increased by a factor of 29 as $E_{1/2}$ increased by 28 mV.

■ CONCLUSIONS

A series of $[(OH_2)(\text{R-terpy})Mn(\mu\text{-O})_2Mn(\text{R-terpy})(OH_2)]^{3+}$ with 4′-substituted terpy (R-terpy) ligands (Chart 1) have been synthesized as a functional OEC model. Mn centers in the cores are crystallographically indistinguishable for **1MeS**, **1Me**, **1EtO**, and **1BuO**, as is the similar case of **1**, whereas they are significantly distinguishable for **1MeO** and **1PrO**. The indistinguishable Mn centers could be caused by rapid electron exchange between the Mn centers to result in the delocalized $Mn(\mu\text{-O})_2Mn$ core. The 4′-substitution on terpy ligands were demonstrated to tune the localized or delocalized core, contributing to magnetic interaction between Mn centers and the redox properties. The catalytic activities of the derivatives on mica for the heterogeneous water oxidation were remarkable changed by the 4′-substituent variation. The second order rate

dx.doi.org/10.1021/ic201797h | Inorg. Chem. 2012, 51, 1530−1539

constant (k_2/mol^{-1} s^{-1}) for the catalysis was indicated to be correlated to $E_{1/2}$ of the Mn^{III}–Mn^{IV}/Mn^{IV}–Mn^{IV} pair; k_2 increased by a factor of 29 as $E_{1/2}$ increased by 28 mV, meaning that $E_{1/2}$ is very critical for the increase of the k_2 value. This result might shed light on difficulty in development of a functional OEC molecule based on manganese-oxo complexes and provide important insight into the OEC structure and the mechanism of water oxidation at OEC.

■ ASSOCIATED CONTENT

Supporting Information

Additional figures. CIF data. This material is available free of charge via the Internet at http://pubs.acs.org.

■ AUTHOR INFORMATION

Corresponding Author

*E-mail: yagi@eng.niigata-u.ac.jp. Fax: +81-25-262-6790.

■ REFERENCES

(1) Wydrzynski, T. J.; Satoh, K. *Photosystem II; The Light-Driven Water: Plastoquinone Oxidoreductase*; Springer: Dordrecht, The Netherlands, 2005.
(2) Dau, H.; Zaharieva, I. *Acc. Chem. Res.* **2009**, *42*, 1861−1870.
(3) Zouni, A.; Witt, H. T.; Kern, J.; Fromme, P.; Krauss, N.; Saenger, W.; Orth, P. *Nature* **2001**, *409*, 739−743.
(4) Ferreira, K. N.; Iverson, T. M.; Maghlaoui, K.; Barber, J.; Iwata, S. *Science* **2004**, *303*, 1831−1838.
(5) Loll, B.; Kern, J.; Saenger, W.; Zouni, A.; Biesiadka, J. *Nature* **2005**, *438*, 1040−1044.
(6) Kamiya, N.; Shen, J.-R. *Proc. Natl. Acad. Sci. U.S.A.* **2003**, *100*, 98−103.
(7) Robblee, J. H.; Cinco, R. M.; Yachandra, V. K. *Biochim. Biophys. Acta, Bioenerg.* **2001**, *1503*, 7−23.
(8) Yano, J.; Kern, J.; Sauer, K.; Latimer, M. J.; Pushkar, Y.; Biesiadka, J.; Loll, B.; Saenger, W.; Messinger, J.; Zouni, A.; Yachandra, V. K. *Science* **2006**, *314*, 821−825.
(9) Umena, Y.; Kawakami, K.; Shen, J.-R.; Kamiya, N. *Nature* **2011**, *473*, 55−60.
(10) Manchanda, R.; Brudvig, G. W.; Crabtree, R. H. *Coord. Chem. Rev.* **1995**, *144*, 1−38.
(11) Carrell, T. G.; Tyryshkin, A. M.; Dismukes, G. C. *JBIC, J. Biol. Inorg. Chem.* **2002**, *7*, 2−22.
(12) Yachandra, V. K.; Sauer, K.; Klein, M. P. *Chem. Rev.* **1996**, *96*, 2927−2950.
(13) Cady, C. W.; Crabtree, R. H.; Brudvig, G. W. *Coord. Chem. Rev.* **2008**, *252*, 444−455.
(14) Wu, A. J.; Penner-Hahn, J. E.; Pecoraro, V. L. *Chem. Rev.* **2004**, *104*, 903−938.
(15) Mukhopadhyay, S.; Mandal, S. K.; Bhaduri, S.; Armstrong, W. H. *Chem. Rev.* **2004**, *104*, 3981−4026.
(16) Mullins, C. S.; Pecoraro, V. L. *Coord. Chem. Rev.* **2008**, *252*, 416−443.
(17) Yagi, M.; Syouji, A.; Yamada, S.; Komi, M.; Yamazaki, H.; Tajima, S. *Photochem. Photobiol. Sci.* **2009**, *8*, 139 −147.
(18) Yamazaki, H.; Shouji, A.; Kajita, M.; Yagi, M. *Coord. Chem. Rev.* **2010**, *254*, 2483−2491.
(19) Yagi, M.; Narita, K. *J. Am. Chem. Soc.* **2004**, *126*, 8084−8085.
(20) Narita, K.; Kuwabara, T.; Sone, K.; Shimizu, K.; Yagi, M. *J. Phys. Chem. B* **2006**, *110*, 23107−23114.
(21) Limburg, J.; Vrettos, J. S.; Liable-Sands, L. M.; Rheingold, A. L.; Crabtree, R. H.; Brudvig, G. W. *Science* **1999**, *283*, 1524−1527.
(22) Limburg, J.; Vrettos, J. S.; Chen, H. Y.; de Paula, J. C.; Crabtree, R. H.; Brudvig, G. W. *J. Am. Chem. Soc.* **2001**, *123*, 423−430.
(23) Poulsen, A. K.; Rompel, A.; McKenzie, C. J. *Angew. Chem., Int. Ed.* **2005**, *44*, 6916−6920.
(24) Naruta, Y.; Sasayama, M.; Sasaki, T. *Angew. Chem., Int. Ed. Engl.* **1994**, *33*, 1839−1841.
(25) Shimazaki, Y.; Nagano, T.; Takesue, H.; Ye, B.-H.; Tani, F.; Naruta, Y. *Angew. Chem., Int. Ed.* **2004**, *43*, 98−100.
(26) Ruettinger, W.; Yagi, M.; Wolf, K.; Bernasek, S.; Dismukes, G. C. *J. Am. Chem. Soc.* **2000**, *122*, 10353−10357.
(27) Yagi, M.; Wolf, K. V.; Baesjou, P. J.; Bernasek, S. L.; Dismukes, G. C. *Angew. Chem., Int. Ed.* **2001**, *40*, 2925−2928.
(28) Brimblecombe, R.; Koo, A.; Dismukes, G. C.; Swiegers, G. F.; Spiccia, L. *J. Am. Chem. Soc.* **2010**, *132*, 2892−2894.
(29) Yagi, M.; Narita, K.; Maruyama, S.; Sone, K.; Kuwabara, T.; Shimizu, K.-i. *Biochim. Biophys. Acta* **2007**, *1767*, 660−665.
(30) Yagi, M.; Toda, M.; Yamada, S.; Yamazaki, H. *Chem. Commun.* **2010**, *46*, 8594−8596.
(31) Yamazaki, H.; Nagata, T.; Yagi, M. *Photochem. Photobiol. Sci.* **2009**, *8*, 204−209.
(32) Hocking, R. K.; Brimblecombe, R.; Chang, L.-Y.; Singh, A.; Cheah, M. H.; Glover, C.; Casey, W. H.; Spiccia, L. *Nat. Chem.* **2011**, *3*, 461−466.
(33) Chen, H.; Tagore, R.; Das, S.; Incarvito, C.; Faller, J. W.; Crabtree, R. H.; Brudvig, G. W. *Inorg. Chem.* **2005**, *44*, 7661−7670.
(34) Andres, P. R.; Lunkwitz, R.; Pabst, G. R.; Bohn, K.; Wouters, D.; Schmatloch, S.; Schubert, U. S. *Eur. J. Org. Chem.* **2003**, 3769−3776.
(35) Chambers, J.; Eaves, B.; Parker, D.; Claxton, R.; Ray, P. S.; Slattery, S. J. *Inorg. Chim. Acta* **2006**, *359*, 2400−2406.
(36) Potts, K. T.; Usifer, D. A.; Guadalupe, A.; Abruna, H. D. *J. Am. Chem. Soc.* **1987**, *109*, 3961−3967.
(37) Constable, E. C.; Ward, M. D. *J. Chem. Soc., Dalton Trans.* **1990**, 1405−1409.
(38) Collomb, M. N.; Deronzier, A.; Richardot, A.; Pecaut, J. *New J. Chem.* **1999**, *23*, 351−353.
(39) Gamelin, D. R.; Kirk, M. L.; Stemmler, T. L.; Pal, S.; Armstrong, W. H.; Pennerhahn, J. E.; Solomon, E. I. *J. Am. Chem. Soc.* **1994**, *116*, 2392−2399.
(40) Cooper, S. R.; Calvin, M. *J. Am. Chem. Soc.* **1977**, *99*, 6623−6630.
(41) The torsion angle is defined by the angle between the planes formed by atoms O(2)−Mn−Mn and atoms Mn−Mn−O(1).
(42) Stebler, M.; A. Ludi, l.; Burgi, H.-B. *Inorg. Chem.* **1986**, *25*, 4743−4750.
(43) Hagen, K. S.; Armstrong, W. H.; Hope, H. *Inorg. Chem.* **1988**, *27*, 967−969.
(44) Goodson, P. A.; Hodgson, D. J.; Glerup, J.; Michelsen, K.; Weihe, H. *Inorg. Chim. Acta* **1992**, *197*, 141−147.
(45) Glerup, J.; Goodson, P. A.; Hazell, A.; Hazell, R.; Hodgson, D. J.; McKenzie, C. J.; Michelsen, K.; Rychlewska, U.; Toftlund, H. *Inorg. Chem.* **1994**, *33*, 4105−4111.
(46) Plaksin, P. M.; Stoufer, R. C.; Mathew, M.; Palenik, G. J. *J. Am. Chem. Soc.* **1972**, *94*, 2121−2122.
(47) Collins, M. A.; Hodgson, D. J.; Michelsen, K.; Towle, D. K. *J. Chem. Soc., Chem. Commun.* **1987**, 1659−1660.
(48) Suzuki, M.; Senda, H.; Kobayashi, Y.; Oshio, H.; Uehara, A. *Chem. Lett.* **1988**, *17*, 1763−1766.
(49) Towle, D. K.; Botsford, C. A.; Hodgson, D. J. *Inorg. Chim. Acta* **1988**, *141*, 167−168.
(50) Goodson, P. A.; Hodgson, D. J.; Michelsen, K. *Inorg. Chim. Acta* **1990**, *172*, 49−57.
(51) Chen, H.; Faller, J. W.; Crabtree, R. H.; Brudvig, G. W. *J. Am. Chem. Soc.* **2004**, *126*, 7345−7349.
(52) Baffert, C.; Romain, S.; Richardot, A.; Lepretre, J.-C.; Lefebvre, B.; Deronzier, A.; Collomb, M.-N. *J. Am. Chem. Soc.* **2005**, *127*, 13694−13704.
(53) Law, N. A.; Kampf, J. W.; Pecoraro, V. L. *Inorg. Chim. Acta* **2000**, *297*, 252−264.